

(ω_1, ω_2) -Temporal random hyperbolic graphs

Sofoclis Zambirinis¹ and Fragkiskos Papadopoulos^{1,*}

¹*Department of Electrical Engineering, Computer Engineering and Informatics,
Cyprus University of Technology, 3036 Limassol, Cyprus*

(Dated: March 27, 2024)

We extend a recent model of temporal random hyperbolic graphs by allowing connections and disconnections to persist across network snapshots with different probabilities, ω_1 and ω_2 . This extension, while conceptually simple, poses analytical challenges involving the Appell F_1 series. Despite these challenges, we are able to analyze key properties of the model, which include the distributions of contact and intercontact durations, as well as the expected time-aggregated degree. The incorporation of ω_1 and ω_2 enables more flexible tuning of the average contact and intercontact durations, and of the average time-aggregated degree, providing a finer control for exploring the effect of temporal network dynamics on epidemic processes. Overall, our results provide new insights into the analysis of temporal networks and contribute to a more general representation of real-world scenarios.

I. INTRODUCTION

Originally motivated by the parsimonious modeling of human contact networks [1–3], a simple model of temporal random hyperbolic graphs has been recently introduced and analyzed, called dynamic- \mathbb{S}^1 [4]. The model has demonstrated the ability to qualitatively and sometimes quantitatively reproduce various dynamical properties observed in real temporal networks. These properties include broad distributions of contact and intercontact durations, broad weight and strength distributions, narrow distributions of shortest time-respecting paths, and formation of recurrent components [4]. In the model, each node is endowed with an expected degree or popularity variable κ and a similarity coordinate θ . Each network snapshot is then independently generated according to the \mathbb{S}^1 model, or equivalently, the hyperbolic \mathbb{H}^2 model [5], where nodes connect with probability $p(\chi) = 1/(1 + \chi^{1/T})$. Here, $\chi \propto \Delta\theta/(\kappa\kappa')$ represents the effective distance between the nodes, $\Delta\theta$ is the nodes' angular similarity distance, κ and κ' are the nodes' expected degrees, and parameter $T \in (0, 1)$ is called network temperature. We note that the dynamic- \mathbb{S}^1 yields realistic dynamical properties only for $T \in (0, 1)$, but not for $T > 1$ [6].

While the snapshots are independently generated in the dynamic- \mathbb{S}^1 , they are not independent as there are correlations among them induced by the nodes' effective distances. For instance, nodes at smaller effective distances have higher chances of being connected in consecutive snapshots. Given the ability of the model to adequately reproduce various dynamical properties of real systems, it has been demonstrated that spreading processes perform remarkably similar in some real networks and their modeled counterparts [4]. Furthermore, the model has already demonstrated its utility in real-world epidemiological studies [7], and has been employed to

justify the meaningful mapping of human proximity networks into hyperbolic spaces [8].

To better capture the average contact and intercontact durations observed in some real systems, the dynamic- \mathbb{S}^1 has been recently extended to account for *link persistence*, where connections and disconnections can persist, i.e., propagate, from one snapshot to the next, irrespective of their effective distance [9–12]. This extension, called ω -dynamic- \mathbb{S}^1 [13], introduces the probability parameter $\omega \in [0, 1)$, dictating the persistence of both connections and disconnections. However, the assumption that links and non-links persist with the same probability may not generally hold in reality. Moreover, because of this assumption, the model does not allow individual tuning of the average contact and intercontact durations, as both are dictated by the same parameter ω .

To address these limitations, here we generalize the model by allowing connections and disconnections to persist with different probabilities, denoted as ω_1 and ω_2 . We refer to the generalized model as (ω_1, ω_2) -dynamic- \mathbb{S}^1 . Even though this generalization is conceptually simple, it poses significant analytical challenges involving the Appell F_1 series—a two-variable generalization of the Gauss hypergeometric function [14]. In our case, these variables involve the persistence probabilities ω_1 and ω_2 . In contrast, the analysis simplifies if $\omega_1 = \omega_2$, requiring only manipulations with the Gauss hypergeometric function [13].

In addition to advancing modeling, incorporating distinct persistence probabilities for connections and disconnections, and understanding their effects on temporal network properties, is important for better understanding the performance of spreading phenomena. This point is illustrated in Fig. 1. The figure shows that stronger link persistence can slow down epidemic spreading, depending on the setting. This occurs as pairs of nodes remain connected for longer durations, effectively reducing their opportunities to connect and infect other nodes. Non-link persistence seems to have a lesser effect, unless it is too strong ($\omega_2 \rightarrow 1$). At the same time, Fig. 1 shows that spreading performance is also affected by the net-

* f.papadopoulos@cut.ac.cy

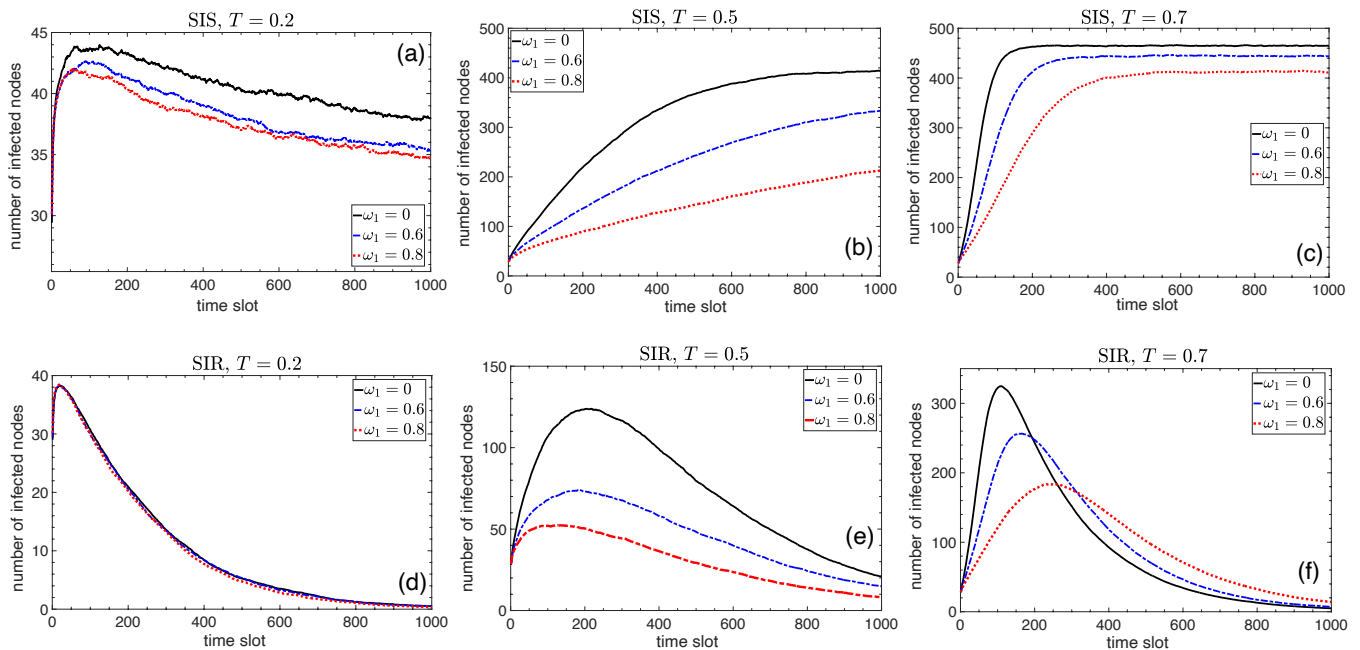


FIG. 1. Exploring epidemic spreading dynamics on temporal networks generated by the (ω_1, ω_2) -dynamic- \mathbb{S}^1 model. Plots (a)-(c) depict the number of infected nodes over time averaged over 100 simulations of the Susceptible-Infected-Susceptible (SIS) model [15]. There are $N = 500$ nodes with a low expected degree $\kappa = \bar{k} = 0.3$, yielding network snapshots in the disconnected regime, as in human proximity networks [3, 4]. Moving from left to right, the network temperature is 0.2, 0.5, and 0.7. Results are presented for different levels of the link persistence probability ω_1 , while in all cases $\omega_2 = 0$. The total number of time slots is $M = 1200$, with the first 200 slots used as a warm-up period for the (ω_1, ω_2) -dynamic- \mathbb{S}^1 to reach a steady state (see text). The subsequent 1000 slots are used for SIS model simulations, starting with 5% of nodes randomly infected, while the infection and recovery probabilities per slot are 0.5 and 0.005, respectively. Plots (d)-(f) show similar dynamics for the Susceptible-Infected-Recovered (SIR) model [15], with all parameters the same as in (a)-(c).

work temperature T , with lower values of T suppressing spreading. This is because lower values of T favor localization of connections in the snapshots, as explained in Sec. II.

Despite the increased complexity introduced by the (ω_1, ω_2) -dynamic- \mathbb{S}^1 , we can still analyze key properties of the model, including its time-dependent and equilibrium connection probability functions, the distributions of contact and intercontact durations, as well as the expected time-aggregated degree, elucidating their dependence on ω_1 , ω_2 , and the network temperature T . We focus on the (inter)contact distributions as they constitute perhaps the most fundamental characteristics affecting the performance of processes running on temporal networks [16–21]. We show that the persistence probabilities ω_1 and ω_2 affect only the averages of these distributions but not their tails. Their tails follow power laws with exponents that depend only on the network temperature T , and these exponents are the same as in the case of $\omega_1 = \omega_2$ [13]. Our results are proven for sufficiently large networks that have evolved for a sufficiently long time to reach a steady state.

The expected time-aggregated degree represents the average number of distinct nodes that a node connects to during an observation period, and is another important characteristic of a temporal network [2, 3]. We

show that as ω_1 or ω_2 increases, or as T decreases, the expected time-aggregated degree decreases, which can slow down spreading (Fig. 1). Having three independent parameters— ω_1 , ω_2 , and T —we can more flexibly adjust the average contact and intercontact durations, as well as the expected time-aggregated degree in the model. This finer control allows for a more nuanced exploration of temporal network dynamics and their impact on spreading processes.

The rest of the paper is structured as follows. In the next section, we provide a brief overview of the \mathbb{S}^1 model. In Sec. III, we present the (ω_1, ω_2) -dynamic- \mathbb{S}^1 model and analyze its connection probability function. In Secs. IV and V, we analyze the contact and intercontact distributions in the model, show their duality, and prove their power law tails. In Sec. VI, we analyze the expected time-aggregated degree. Finally, in Section VII, we discuss open problems and conclude the paper.

II. PRELIMINARIES

In the \mathbb{S}^1 model [5], each node is associated with a pair of hidden (or latent) variables (κ, θ) . The hidden variable κ represents the *popularity* of the node, and is proportional to the node’s expected degree in the network. The

hidden variable θ represents the angular *similarity* coordinate of the node on a circle of radius $R = N/2\pi$, where N is the total number of nodes [22].

To generate a network that has size N , average node degree \bar{k} , and temperature $T \in (0, 1)$, we perform the following steps:

- (i) For each node $i \in \{1, 2, \dots, N\}$, we sample its degree variable κ_i from a probability density function (PDF) $\rho(\kappa)$, and its angular coordinate θ_i uniformly at random from $[0, 2\pi]$.
- (ii) We connect every pair of nodes i and j according to the Fermi-Dirac connection probability

$$p_{ij} = \frac{1}{1 + \chi_{ij}^{1/T}}, \quad (1)$$

where χ_{ij} is the effective distance between nodes i and j ,

$$\chi_{ij} = \frac{R\Delta\theta_{ij}}{\mu\kappa_i\kappa_j}. \quad (2)$$

In the above relation, $\Delta\theta_{ij} = \pi - |\pi - |\theta_i - \theta_j||$ represents the similarity distance between nodes i and j . $\Delta\theta$ follows a uniform distribution on $[0, \pi]$, i.e., its PDF is $f(\Delta\theta) = 1/\pi$.

We are interested in sparse networks, where $N \gg \bar{k}$. In such cases, the resulting degree distribution in the network has a similar form as $\rho(\kappa)$ [23]. We also note that smaller values of the temperature T favor connections at smaller effective distances, i.e., the localization of connections, increasing clustering in the network. Finally, parameter μ in Eq. (2) is derived from the requirement that the expected degree in the network is \bar{k} , yielding

$$\mu = \frac{\bar{k} \sin(T\pi)}{2\bar{k}^2 T\pi}, \quad (3)$$

where $\bar{\kappa} = \int \kappa \rho(\kappa) d\kappa$.

The \mathbb{S}^1 model is isomorphic to random hyperbolic graphs (RHGs) after a transformation of the degree variables κ to radial coordinates r on the hyperbolic disk (see Ref. [5] for more details).

III. (ω_1, ω_2) -DYNAMIC- \mathbb{S}^1

The (ω_1, ω_2) -dynamic- \mathbb{S}^1 model generates a series of network snapshots, G_t , $t = 1, \dots, M$, where M represents the total number of time slots. In the model, there are N nodes that are assigned hidden variables (κ, θ) as in the \mathbb{S}^1 model, which remain fixed throughout the snapshots. The temperature $T \in (0, 1)$ and the persistence probabilities $\omega_1 \in [0, 1)$ and $\omega_2 \in [0, 1)$ are also fixed. While each snapshot G_t can potentially have a different average degree \bar{k}_t , to facilitate the analysis, we assume here a uniform average degree, i.e., $\bar{k}_t = \bar{k}$, $\forall t$. Therefore, the model parameters are $N, M, \rho(\kappa), \bar{k}, T, \omega_1, \omega_2$.

Let

$$e_{ij}^{(t)} = \begin{cases} 1 & \text{if nodes } i \text{ and } j \text{ are connected at time } t, \\ 0 & \text{otherwise.} \end{cases}$$

The snapshots in the model are generated according to the following rules:

- (1) Snapshot G_1 is generated according to the \mathbb{S}^1 model, except that the connection probability is not given by Eq. (1) but by

$$\tilde{p}_{ij} = \frac{1}{1 + \left(\frac{1-\omega_2}{1-\omega_1}\right)\chi_{ij}^{1/T}}. \quad (4)$$

- (2) At each time step $t = 2, \dots, M$, snapshot G_t starts with N disconnected nodes.
- (3) Each pair of nodes i, j in snapshot G_t connects according to the following conditional connection probabilities:

$$\mathbb{P}[e_{ij}^{(t)} = 1 | e_{ij}^{(t-1)} = 1] = \omega_1 + (1 - \omega_1)\tilde{p}_{ij}, \quad (5)$$

$$\mathbb{P}[e_{ij}^{(t)} = 1 | e_{ij}^{(t-1)} = 0] = (1 - \omega_2)\tilde{p}_{ij}. \quad (6)$$

- (4) At time $t + 1$, the process is repeated to generate snapshot G_{t+1} .

Equation (5) represents the scenario in which the pair i, j is connected in the previous time slot $t - 1$. In this case, the pair remains connected in slot t either because the connection persists from $t - 1$ (with probability ω_1) or because the connection is established according to \tilde{p}_{ij} (with probability $1 - \omega_1$). Equation (6) represents the situation where the pair i, j is disconnected in $t - 1$. In this case, the pair can establish a connection in slot t if the disconnection does not persist from $t - 1$ (with probability $1 - \omega_2$), and the connection is established according to \tilde{p}_{ij} .

As we show below, the choice of the connection probability function in Eq. (4) ensures that the equilibrium connection probability in the model is given by Eq. (1). Consequently, snapshots generated by the model are equivalent in equilibrium to RHGs, despite the dependencies introduced among them by the persistence probabilities ω_1 and ω_2 .

Equilibrium connection probability. We can express the unconditional connection probability for any node pair i, j at time $t = 2, 3, \dots$, as follows:

$$\begin{aligned} \mathbb{P}[e_{ij}^{(t)} = 1] &= \mathbb{P}[e_{ij}^{(t)} = 1 | e_{ij}^{(t-1)} = 1] \times \mathbb{P}[e_{ij}^{(t-1)} = 1] \\ &+ \mathbb{P}[e_{ij}^{(t)} = 1 | e_{ij}^{(t-1)} = 0] \times (1 - \mathbb{P}[e_{ij}^{(t-1)} = 1]) \\ &= [\omega_1 + (\omega_2 - \omega_1)\tilde{p}_{ij}] \times \mathbb{P}[e_{ij}^{(t-1)} = 1] \\ &+ (1 - \omega_2)\tilde{p}_{ij}. \end{aligned} \quad (7)$$

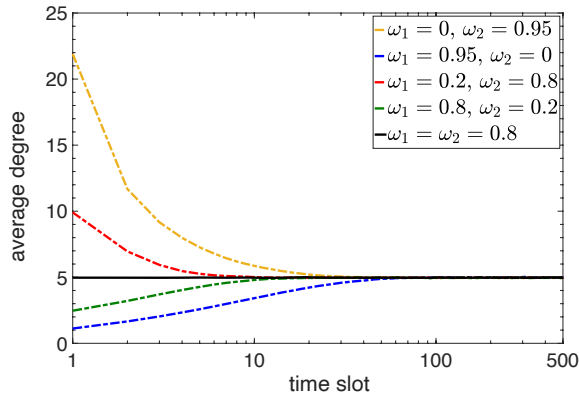


FIG. 2. Average snapshot degree as a function of time in the (ω_1, ω_2) -dynamic- \mathbb{S}^1 . The network consists of $N = 500$ nodes, the number of time slots is $M = 500$, the network temperature is $T = 0.5$, and all nodes have the same expected degree $\kappa = \bar{k} = 5$. Results are shown for different values of the persistence probabilities ω_1 and ω_2 , and represent averages across 100 simulation runs. In all cases, the average snapshot degree converges to its target value $\bar{k} = 5$ before slot 100. Convergence is slower the bigger the difference between ω_1 and ω_2 . The x -axis is on a logarithmic scale.

Solving the above recurrence relation for $\mathbb{P}[e_{ij}^{(t)} = 1]$, with the initial condition $\mathbb{P}[e_{ij}^{(1)} = 1] = \tilde{p}_{ij}$, yields

$$\mathbb{P}[e_{ij}^{(t)} = 1] = \frac{B(1 - A^{t-1})}{1 - A} + \tilde{p}_{ij}A^{t-1}, \quad (8)$$

where $A = \omega_1 + (\omega_2 - \omega_1)\tilde{p}_{ij}$, and $B = (1 - \omega_2)\tilde{p}_{ij}$.

We note that $0 \leq A < 1$. Hence, as t tends to infinity, A^{t-1} converges to 0. Therefore, assuming that the system has evolved for a sufficiently long time, we can drop the superscript t from Eq. (8), and write the *steady-state* or *equilibrium* connection probability:

$$\begin{aligned} \mathbb{P}[e_{ij} = 1] &= \frac{B}{1 - A} \\ &= \frac{(1 - \omega_2)\tilde{p}_{ij}}{1 - \omega_1 + (\omega_1 - \omega_2)\tilde{p}_{ij}} \\ &= \frac{1}{1 + \chi_{ij}^{1/T}} \\ &= p_{ij}. \end{aligned} \quad (9)$$

Thus, the equilibrium connection probability in the model is indeed as in Eq. (1). The convergence to equilibrium depends on the values of ω_1 and ω_2 and generally

occurs rapidly. However, it slows down as the difference between ω_1 and ω_2 increases. Figure 2 illustrates this point. In the next section, we analyze the distribution of contact durations in the model.

IV. DISTRIBUTION OF CONTACT DURATIONS

For our analysis, we assume that the system has reached equilibrium, and we consider its evolution in a time window of τ slots.

To derive the contact distribution, we need to consider the probability of observing a sequence of exactly t consecutive time slots where two nodes i and j with hidden degrees κ_i and κ_j and angular distance $\Delta\theta_{ij}$ are connected. Any such sequence should be enclosed within two slots where the two nodes are not connected. That is, we ignore for now the boundary cases where the first or last of the t slots starts or ends at the beginning or end of the observation period τ . Therefore, t ranges from 1 to $\tau - 2$. We denote this probability by $r_c(t; \kappa_i, \kappa_j, \Delta\theta_{ij})$.

We note that given a sequence of length t , there exist $\tau - t - 1$ possible starting positions for this sequence. For example, if $t = 3$, the nodes can be disconnected in slot $s - 1$, connected in slots $s, s + 1, s + 2$, and disconnected in slot $s + 3$, where s ranges from 2 to $\tau - 3$. Consequently, the probability of observing a slot where a sequence of length t can start is

$$g_\tau(t) = \frac{\tau - t - 1}{\tau}. \quad (10)$$

Furthermore, we observe the following:

- (i) In equilibrium, the probability that two nodes i and j are disconnected in a slot s is $1 - p_{ij}$, where p_{ij} is given by Eq. (9).
- (ii) Given that they are disconnected in slot s , the probability that i and j are connected in slot $s + 1$ is $(1 - \omega_2)\tilde{p}_{ij}$, where \tilde{p}_{ij} is given by Eq. (4).
- (iii) Given that they are connected in slot $s + 1$, the probability that i and j remain connected in slots $s + 2, \dots, s + t$ is $[\omega_1 + (1 - \omega_1)\tilde{p}_{ij}]^{t-1}$.
- (iv) Finally, given that they are connected in slot $s + t$, the probability that i and j are disconnected in slot $s + t + 1$ is $(1 - \omega_1)(1 - \tilde{p}_{ij})$.

The probability $r_c(t; \kappa_i, \kappa_j, \Delta\theta_{ij})$ is obtained by multiplying $g_\tau(t)$ with the probabilities described in points (i) to (iv) above,

$$r_c(t; \kappa_i, \kappa_j, \Delta\theta_{ij}) = g_\tau(t)(1 - \omega_1)(1 - \omega_2)(1 - p_{ij})\tilde{p}_{ij}(1 - \tilde{p}_{ij})[\omega_1 + (1 - \omega_1)\tilde{p}_{ij}]^{t-1}. \quad (11)$$

The contact distribution, denoted as $P_c(t)$ and defined

for $t \geq 1$, is given by

$$P_c(t) = \frac{r_c(t)}{\sum_j r_c(j)} \propto r_c(t). \quad (12)$$

In the last expression, $r_c(t)$ is determined by removing

the conditions on κ_i , κ_j , and $\Delta\theta_{ij}$ from Eq. (11),

$$r_c(t) = \int \int \int r_c(t; \kappa, \kappa', \Delta\theta) \rho(\kappa) \rho(\kappa') f(\Delta\theta) d\kappa d\kappa' d\Delta\theta. \quad (13)$$

We note that in practice, given a set of nonzero contact durations, the empirical $P_c(t)$ is determined by the ratio

$n_t / \sum_j n_j$, where n_t represents the number of contact durations in the set with length t .

Removing the condition on $\Delta\theta_{ij}$ from Eq. (11), yields

$$\begin{aligned} r_c(t; \kappa_i, \kappa_j) &= \frac{1}{\pi} \int_0^\pi r_c(t; \kappa_i, \kappa_j, \Delta\theta) d\Delta\theta \\ &= g_\tau(t) \frac{2\mu\kappa_i\kappa_j T}{N} (1-\omega_1)^{1+T} (1-\omega_2)^{1-T} \omega_1^{t-1} \int_{u_0^{ij}}^1 u^{-T} (1-u)^{1+T} \left(1 - \frac{\omega_1-1}{\omega_1} u\right)^{t-1} \left(1 - \frac{\omega_2-\omega_1}{1-\omega_1} u\right)^{-1} du, \\ \text{where } u_0^{ij} &= \frac{1}{1 + \left(\frac{1-\omega_2}{1-\omega_1}\right) \left(\frac{N}{2\mu\kappa_i\kappa_j}\right)^{1/T}}. \end{aligned} \quad (14)$$

To obtain the above relation, we performed the change of integration variable $u = 1/[1 + (\frac{1-\omega_2}{1-\omega_1})(\frac{N\Delta\theta}{2\pi\mu\kappa_i\kappa_j})^{1/T}]$.

Now, for sufficiently large network sizes N , u_0^{ij} tends

to zero. This allows us to remove the condition on κ_i and κ_j from Eq. (14), and write, *irrespective of the form of* $\rho(\kappa)$,

$$r_c(t) \approx g_\tau(t) \frac{2\mu\bar{\kappa}^2 T}{N} (1-\omega_1)^{1+T} (1-\omega_2)^{1-T} \omega_1^{t-1} \int_0^1 u^{-T} (1-u)^{1+T} \left(1 - \frac{\omega_1-1}{\omega_1} u\right)^{t-1} \left(1 - \frac{\omega_2-\omega_1}{1-\omega_1} u\right)^{-1} du. \quad (15)$$

The integral in Eq. (15) can be evaluated numerically. However, we observe that it is in a form suitable for representation using the Appell F_1 series [24]. This representation will be employed below to deduce the behavior of the tail of $r_c(t)$. In particular, Émile Picard discovered

in 1881 that the Appell F_1 series, whose definition is provided in Appendix A, has the following one-dimensional Euler-type integral representation (cf. section 5.8.2 of Ref. [24]):

$$F_1[a, b_1, b_2, c; x, y] = \frac{\Gamma(c)}{\Gamma(a)\Gamma(c-a)} \int_0^1 u^{a-1} (1-u)^{c-a-1} (1-xu)^{-b_1} (1-yu)^{-b_2} du. \quad (16)$$

The above relation is valid for $c > a > 0$, while Γ is the gamma function. Utilizing this representation with $\alpha = 1 - T$, $b_1 = 1 - t$, $b_2 = 1$, $c = 3$, $x = \frac{\omega_1-1}{\omega_1}$, and

$y = \frac{\omega_2-\omega_1}{1-\omega_1}$, substituting μ with its expression in Eq. (3), and employing the identity $\frac{\pi}{\sin(T\pi)} = \Gamma(1-T)\Gamma(T)$, we can rewrite Eq. (15), as

$$\begin{aligned} r_c(t) &\approx g_\tau(t) \frac{\bar{k}T(1+T)}{2N} (1-\omega_1)^{1+T} (1-\omega_2)^{1-T} \omega_1^{t-1} F_1\left[1-T, 1-t, 1, 3; \frac{\omega_1-1}{\omega_1}, \frac{\omega_2-\omega_1}{1-\omega_1}\right] \\ &= g_\tau(t) \frac{\bar{k}T(1+T)}{2N} (1-\omega_1)^{2+T} (1-\omega_2)^{-T} F_1\left[2+T, 1-t, 1, 3; 1-\omega_1, \frac{\omega_1-\omega_2}{1-\omega_2}\right]. \end{aligned} \quad (17)$$

The last equality is obtained by performing the change of variable $v = 1 - u$ in the integral of Eq. (16), or equivalently, by applying the transformation given by Eq. (1) in section 5.11 of Ref. [24]. For $\omega_1 = \omega_2 = \omega$ the last F_1 function in Eq. (17) degenerates to the Gauss hypergeometric function ${}_2F_1[2+T, 1-t, 3; 1-\omega]$ (see Appendix A for its definition), and we recover the relation for $r_c(t)$

$$r_c^b(t; \kappa_i, \kappa_j, \Delta\theta_{ij}) = \frac{1}{\tau} (1 - \omega_1) p_{ij} (1 - \tilde{p}_{ij}) [\omega_1 + (1 - \omega_1) \tilde{p}_{ij}]^{t-1}, \quad (18)$$

for $t = 1, \dots, \tau - 1$. Similarly, the analysis did not consider the case where the last slot in the sequence of t slots, during which two nodes are connected, finishes at the end of the observation period. It is easy to see that the probability of observing this event is also given by

found in Ref. [13].

Boundary cases. The preceding analysis did not consider the boundary case where the first slot in the sequence of t slots, during which two nodes are connected, starts at the beginning of the observation period τ . In this case, $g_\tau(t) = 1/\tau$, and the probability of observing this event for two nodes i and j is given by

$$\begin{aligned} r_c^b(t) &\approx \frac{2}{\tau} \frac{2\mu\bar{\kappa}^2 T}{N} (1 - \omega_1)^T (1 - \omega_2)^{1-T} \omega_1^{t-1} \int_0^1 u^{-T} (1-u)^T \left(1 - \frac{\omega_1 - 1}{\omega_1} u\right)^{t-1} \left(1 - \frac{\omega_2 - \omega_1}{1 - \omega_1} u\right)^{-1} du \\ &= \frac{2}{\tau} \frac{\bar{k} T}{N} (1 - \omega_1)^{1+T} (1 - \omega_2)^{-T} F_1[1+T, 1-t, 1, 2; 1 - \omega_1, \frac{\omega_1 - \omega_2}{1 - \omega_2}]. \end{aligned} \quad (19)$$

We note that for any finite t , $r_c^b(t)$ tends to zero as $\tau \rightarrow \infty$. However, as t approaches τ , the contribution of these boundary cases becomes significant. Accounting for these cases, the combined probability of observing a sequence of t consecutive slots in which two nodes are connected is given by

$$\tilde{r}_c(t) = r_c(t) + r_c^b(t), \quad (20)$$

for $t = 1, \dots, \tau - 1$.

Eq. (18).

Following the same procedure to remove the conditions on κ_i , κ_j , and $\Delta\theta_{ij}$, and employing the same transformations as before, we can write that the total probability for these two cases is given by

The final boundary case occurs when two nodes i and j remain connected for the entire observation period τ . The probability of observing this case is

$$r_c^b(\tau; \kappa_i, \kappa_j, \Delta\theta_{ij}) = \frac{1}{\tau} p_{ij} [\omega_1 + (1 - \omega_1) \tilde{p}_{ij}]^{\tau-1}. \quad (21)$$

Removing the conditions on κ_i , κ_j , and $\Delta\theta_{ij}$, and employing the same transformations as before, gives

$$\begin{aligned} r_c^b(\tau) &\approx \frac{1}{\tau} \frac{2\mu\bar{\kappa}^2 T}{N} \left(\frac{1 - \omega_2}{1 - \omega_1}\right)^{1-T} \omega_1^{\tau-1} \int_0^1 u^{-T} (1-u)^{T-1} \left(1 - \frac{\omega_1 - 1}{\omega_1} u\right)^{\tau-1} \left(1 - \frac{\omega_2 - \omega_1}{1 - \omega_1} u\right)^{-1} du \\ &= \frac{1}{\tau} \frac{\bar{k}}{N} \left(\frac{1 - \omega_1}{1 - \omega_2}\right)^T F_1[T, 1 - \tau, 1, 1; 1 - \omega_1, \frac{\omega_1 - \omega_2}{1 - \omega_2}]. \end{aligned} \quad (22)$$

We note that previous studies related to the dynamic-S¹ model [4, 13] have not considered the above boundary cases. In Fig. 3, we validate the above analysis with simulations, while also taking into account the boundary cases. In all cases, we calculate $r_c(t)$ and $r_c^b(t)$ using their integral representations, as we have found it more efficient than utilizing the corresponding Appell F_1 series.

Average contact duration. It is evident from our analysis and Fig. 3 that all three parameters— ω_1 , ω_2 , and T —affect the contact distribution. In Fig. 4, we investigate how these parameters affect the average contact duration.

We see from Fig. 4 that the average contact duration increases as either ω_1 or ω_2 increases, with the rate of

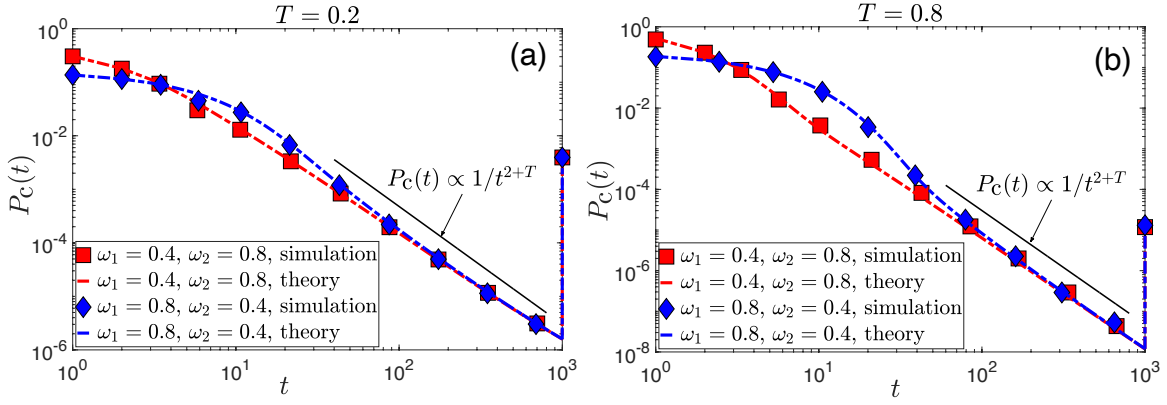


FIG. 3. Distribution of contact durations in simulated networks with the (ω_1, ω_2) -dynamic- S^1 model vs. theoretical predictions. The latter are given by $P_c(t) = \tilde{r}_c(t) / \sum_{j=1}^{\tau} \tilde{r}_c(j)$, where $\tilde{r}_c(t)$ is given by Eq. (20) for $t = 1, \dots, \tau - 1$, and by Eq. (22) for $t = \tau$ (yielding the rightmost point on the plots). The number of nodes is $N = 500$, the average node degree is $\bar{k} = 5$, and all nodes have the same expected degree $\kappa = \bar{k}$. The total number of time slots is $M = 1200$, with the first 200 slots used as a warm-up period. Empirical distributions are computed over the subsequent $\tau = 1000$ slots. The network temperature in (a) is $T = 0.2$, and in (b) $T = 0.8$. Results are presented for two combinations of the persistence probabilities ω_1 and ω_2 . The simulations are averaged over 10 runs, and empirical distributions are logarithmically binned, excluding the rightmost point. Theoretical predictions are represented by dashed lines. All axes use a logarithmic scale.

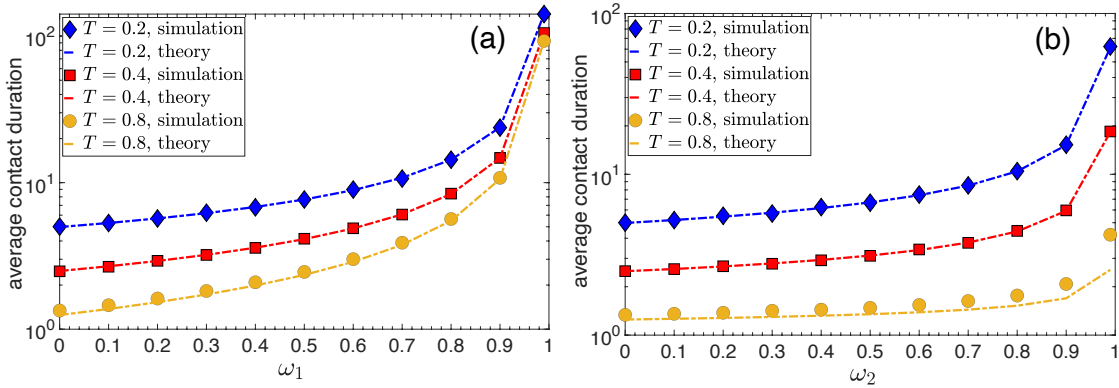


FIG. 4. Average contact duration vs. ω_1 , ω_2 , and T . Plot (a) shows the average contact duration in time slots as a function of the persistence probability of connections ω_1 . The persistence probability of disconnections, ω_2 , is set to zero. Results are shown for different values of the network temperature T . All other parameters are the same as in Fig. 3. The dashed lines depict theoretical predictions given by $\bar{t}_c = \sum_{t=1}^{\tau} t P_c(t)$, where $P_c(t)$ is computed as in Fig. 3. Plot (b) is similar to (a), except that ω_1 is set to zero, and we vary ω_2 . The y -axes use a logarithmic scale. Deviations of analytical predictions from simulation results are due to finite network size effects and are more pronounced for values of T or ω_2 closer to 1.

increase becoming more pronounced as these parameters approach 1. Moreover, we observe that the average contact duration is more sensitive to and increases more rapidly with ω_1 than with ω_2 . This is expected, as ω_1 directly impacts the probability that two nodes remain connected, given by Eq. (5). In particular, as $\omega_1 \rightarrow 1$, the probability in Eq. (5) approaches 1, irrespective of the value of ω_2 . On the other hand, ω_2 indirectly affects this probability via \tilde{p}_{ij} (Eq. (4)). Indeed, as $\omega_2 \rightarrow 1$, $\tilde{p}_{ij} \rightarrow 1$, and Eq. (5) tends to 1, irrespective of the value of ω_1 . In other words, as $\omega_1 \rightarrow 1$ or $\omega_2 \rightarrow 1$, the contact distribution degenerates to $P_c(t) \rightarrow 1$ for $t = \tau$, and $P_c(t) \rightarrow 0$, for $t < \tau$, while the average contact duration tends to the value of the observation interval τ . This convergence

occurs faster with $\omega_1 \rightarrow 1$ than with $\omega_2 \rightarrow 1$.

Lastly, Fig. 4 shows that the average contact duration also increases as T decreases. A lower T favors connections at smaller effective distances, thereby increasing the probability that connected pairs remain connected. For $T \rightarrow 0$, we obtain the same result as in the case of $\omega_1 \rightarrow 1$ or $\omega_2 \rightarrow 1$.

Tail of the contact distribution. We conclude our analysis in this section by deducing the behavior of $P_c(t)$ at large t . To this end, we utilize an asymptotic result given by Eq. (20) in section 3.5.1 of Ref. [25]. This result states that for $x < 0$ and $|y| < 1$, we can express the Appell function $F_1[a, b + \lambda, b', c; x, y]$ as a sum of Gauss hypergeometric functions,

$$F_1[a, b + \lambda, b', c; x, y] = \sum_{n=0}^{m-1} \binom{-b'}{n} \frac{(a)_n (-y)^n}{(c)_n} {}_2F_1[b + \lambda, a + n, c + n; x] + O(\lambda^{-m-a}), \quad (23)$$

where $(q)_n$ denotes the Pochhammer symbol, defined as: $(q)_n = 1$ for $n = 0$ and $(q)_n = q(q+1)\dots(q+n-1)$ for

$n > 0$. Furthermore, we utilize the transformation given by Eq. (2) in section 5.11 of Ref. [24], which states that

$$F_1[a, b, b', c; x, y] = (1-x)^{-a} F_1[a, c-b-b', b', c; \frac{x}{x-1}, \frac{y-x}{1-x}]. \quad (24)$$

Using the above transformation, we can rewrite the F_1

function in Eq. (17), which we refer to as h_1 , as

$$h_1 := F_1[2+T, 1-t, 1, 3; 1-\omega_1, \frac{\omega_1-\omega_2}{1-\omega_2}] = \omega_1^{-(2+T)} F_1[2+T, 1+t, 1, 3; 1-\frac{1}{\omega_1}, 1-\frac{1-\omega_1}{\omega_1(1-\omega_2)}]. \quad (25)$$

Now, using Eq. (23) with $a = 2+T$, $b = 1$, $\lambda = t$, $b' = 1$,

$c = 3$, $x = 1 - \frac{1}{\omega_1}$, and $y = 1 - \frac{1-\omega_1}{\omega_1(1-\omega_2)}$, we can write

$$h_1 = \omega_1^{-(2+T)} \sum_{n=0}^{m-1} \frac{(2+T)_n}{(3)_n} \left(1 - \frac{1-\omega_1}{\omega_1(1-\omega_2)}\right)^n {}_2F_1[1+t, 2+T+n, 3+n; 1-\frac{1}{\omega_1}] + O\left(\frac{1}{t^{2+T+m}}\right). \quad (26)$$

To write the above relation, we also utilized that $\binom{-1}{n} = (-1)^n$ for $n \in \mathbb{N}$.

As shown in Appendix B, the ${}_2F_1$ function inside the sum in Eq. (26) can be approximated for large t as

$${}_2F_1[1+t, 2+T+n, 3+n; 1-\frac{1}{\omega_1}] \approx \frac{\Gamma(3+n)(1/\omega_1-1)^{-(2+T+n)}}{\Gamma(1-T)} \frac{1}{t^{2+T+n}}. \quad (27)$$

Consequently, at large t , the term corresponding to $n = 0$ in Eq. (26) dominates, and we can approximate h_1 as

$$h_1 \approx \frac{2(1-\omega_1)^{-(2+T)}}{\Gamma(1-T)} \frac{1}{t^{2+T}}. \quad (28)$$

This approximation is validated in Fig. 5.

We note that Eq. (26) holds for $x = 1 - \frac{1}{\omega_1} < 0$ and $|y| = \left|1 - \frac{1-\omega_1}{\omega_1(1-\omega_2)}\right| < 1$. The first inequality always holds (as $\omega_1 < 1$), while the second imposes the constraint $\omega_2 < \frac{3\omega_1-1}{2\omega_1}$. Additionally, the approximation in Eq. (27) requires $|1 - \frac{1}{\omega_1}| < 1$, which imposes the constraint $\omega_1 > 1/2$. Combined, these constraints define the region \mathcal{R}_1 of ω_1 and ω_2 depicted in Fig. 6, for which the preceding analysis leading to Eq. (28) holds. However,

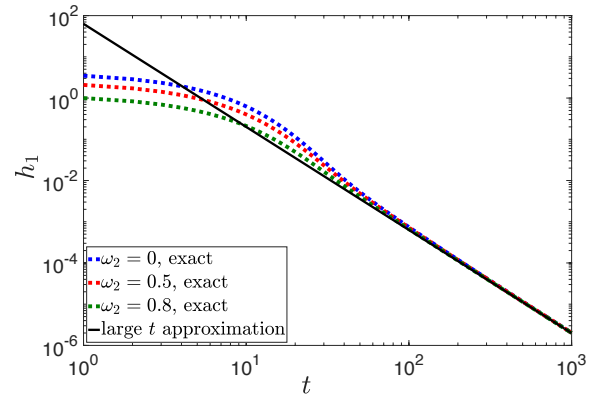


FIG. 5. Function h_1 in Eq. (25) (dotted lines) vs. the approximation for large t in Eq. (28) (solid line). Results are shown for different values of ω_2 , while $\omega_1 = 0.8$ and $T = 0.5$. All axes use a logarithmic scale.

in Appendix B, we prove that Eq. (28), which is established here for the region \mathcal{R}_1 , holds in fact true for any combination of $\omega_1, \omega_2 \in [0, 1)$.

The above analysis (and the corresponding analysis in Appendix B) can be repeated for the function F_1 in Eq. (19), which corresponds to the boundary cases. This

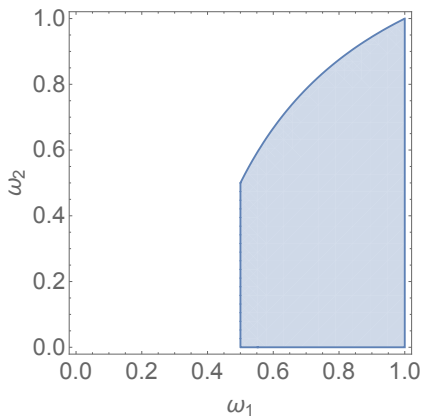


FIG. 6. Region $\mathcal{R}_1 := \{(\omega_1, \omega_2) \in \mathbb{R}^2 \mid \frac{1}{2} < \omega_1 < 1, 0 \leq \omega_2 < \frac{3\omega_1 - 1}{2\omega_1}\}$.

yields, for large t ,

$$F_1[1+T, 1-t, 1, 2; 1-\omega_1, \frac{\omega_1-\omega_2}{1-\omega_2}] \approx \frac{(1-\omega_1)^{-(1+T)}}{\Gamma(1-T)} \frac{1}{t^{1+T}}. \quad (29)$$

Utilizing the approximations given by Eqs. (28) and (29), we can approximate $\tilde{r}_c(t)$ in Eq. (20) for large t as

$$\tilde{r}_c(t) \approx \frac{\bar{k}T}{N} \frac{(1-\omega_2)^{-T}}{\Gamma(1-T)} \left[g_\tau(t) \frac{(1+T)}{t^{2+T}} + \frac{2}{\tau} \frac{1}{t^{1+T}} \right] \propto \frac{1+T+(1-T)t/\tau}{t^{2+T}}. \quad (30)$$

We can now see that for $t \ll \tau$, such that $t/\tau \approx 0$, $\tilde{r}_c(t)$, and consequently, the contact distribution $P_c(t)$, decay according to the power law $1/t^{2+T}$. However, as t approaches the value of the observation interval τ , the decay deviates from pure power-law behavior. This deviation is solely a consequence of the finiteness of the observa-

tion interval. The scaling $P_c(t) \propto 1/t^{2+T}$ is illustrated in Fig. 3. Next, we analyze the intercontact distribution.

V. DISTRIBUTION OF INTERCONTACT DURATIONS

The intercontact distribution is dual to the contact distribution, and to derive it, we follow a similar procedure. Specifically, here we need to consider the probability of observing a sequence of exactly t consecutive time slots where two nodes i and j with hidden degrees κ_i and κ_j and angular distance $\Delta\theta_{ij}$ are disconnected. Any such sequence should be enclosed within two slots where the two nodes are connected. Here we do not consider boundary cases, where the first or last of the t slots starts or ends at the beginning or end of the observation period τ , since by definition an intercontact duration should be enclosed within two contacts. Therefore, t ranges from 1 to $\tau - 2$. We denote the above probability by $r_{ic}(t; \kappa_i, \kappa_j, \Delta\theta_{ij})$.

We observe the following:

- (i) In equilibrium, the probability that two nodes i and j are connected in a slot s is p_{ij} , where p_{ij} is given by Eq. (9).
- (ii) Given that they are connected in slot s , the probability that i and j are disconnected in slot $s+1$ is $(1-\omega_1)(1-\tilde{p}_{ij})$, where \tilde{p}_{ij} is given by Eq. (4).
- (iii) Given that they are disconnected in slot $s+1$, the probability that i and j remain disconnected in slots $s+2, \dots, s+t$ is $[1-(1-\omega_2)\tilde{p}_{ij}]^{t-1}$.
- (iv) Finally, given that they are disconnected in slot $s+t$, the probability that i and j are connected in slot $s+t+1$ is $(1-\omega_2)\tilde{p}_{ij}$.

The probability $r_{ic}(t; \kappa_i, \kappa_j, \Delta\theta_{ij})$ is obtained by multiplying $g_\tau(t)$ in Eq. (10) with the probabilities described in points (i) to (iv) above,

$$r_{ic}(t; \kappa_i, \kappa_j, \Delta\theta_{ij}) = g_\tau(t)(1-\omega_1)(1-\omega_2)p_{ij}\tilde{p}_{ij}(1-\tilde{p}_{ij})[1-(1-\omega_2)\tilde{p}_{ij}]^{t-1}. \quad (31)$$

The intercontact distribution, denoted as $P_{ic}(t)$ and defined for $t \geq 1$, is given by

$$P_{ic}(t) = \frac{r_{ic}(t)}{\sum_j r_{ic}(j)} \propto r_{ic}(t), \quad (32)$$

where $r_{ic}(t)$ is determined by removing the conditions on

κ_i , κ_j , and $\Delta\theta_{ij}$ from Eq. (31),

$$r_{ic}(t) = \int \int \int r_{ic}(t; \kappa, \kappa', \Delta\theta) \rho(\kappa) \rho(\kappa') f(\Delta\theta) d\kappa d\kappa' d\Delta\theta. \quad (33)$$

Following the same procedure as before to remove the conditions on κ_i , κ_j , and $\Delta\theta_{ij}$, and employing the same transformations, we can write that for sufficiently large networks

$$\begin{aligned}
r_{\text{ic}}(t) &\approx g_\tau(t) \frac{2\mu\bar{\kappa}^2 T}{N} (1-\omega_1)^T (1-\omega_2)^{2-T} \int_0^1 u^{1-T} (1-u)^T [1 - (1-\omega_2)u]^{t-1} \left(1 - \frac{\omega_2 - \omega_1}{1-\omega_1} u\right)^{-1} du \\
&= g_\tau(t) \frac{\bar{k}T(1-T)}{2N} (1-\omega_1)^T (1-\omega_2)^{2-T} F_1[2-T, 1-t, 1, 3; 1-\omega_2, \frac{\omega_2 - \omega_1}{1-\omega_1}].
\end{aligned} \tag{34}$$

We can observe the perfect duality between $r_{\text{ic}}(t)$ and $r_c(t)$, in the sense that Eq. (34) becomes Eq. (17), if we exchange ω_2 with ω_1 , T with $-T$, and multiply the resulting relation by -1 . The above analysis is validated in Fig. 7.

Average intercontact duration. In Fig. 8, we investigate how parameters ω_1 , ω_2 , and T affect the average intercontact duration. As with the case of the average contact duration, we see that the average intercontact duration also increases with ω_1 or ω_2 , with the rate of increase becoming more pronounced as these parameters approach 1. Further, we see that the increase is more rapid with ω_2 than with ω_1 , especially as these parameters approach 1. This is expected, as ω_2 directly impacts the probability that two nodes remain disconnected via Eq. (6). It can be shown that as ω_2 approaches 1, $P_{\text{ic}}(t)$ becomes proportional to $g_\tau(t)$, and the average intercontact duration tends to $\tau/3$. On the other hand, as ω_1 approaches 1, $P_{\text{ic}}(t)$ becomes proportional to $g_\tau(t) {}_2F_1[1-T, 1-t, 2; 1-\omega_2]$, while the average intercontact duration is upper-bounded by $\tau/3$. The average intercontact duration also increases with T , while remaining upper-bounded by $\tau/3$. This is because higher values of T increase randomness in the connections, thereby reducing the probability of pairs reconnecting.

Tail of the intercontact distribution. Finally, given the duality between Eqs. (34) and (17), we can follow exactly the same procedure as in the case of Eq. (17), to show that for large t , $r_{\text{ic}}(t)$ can be approximated as

$$r_{\text{ic}}(t) \approx g_\tau(t) \frac{\bar{k}T(1-T)(1-\omega_1)^T}{N\Gamma(1+T)} \frac{1}{t^{2-T}} \propto \frac{g_\tau(t)}{t^{2-T}}. \tag{35}$$

$$r_0(\kappa_i, \kappa_j) = \frac{2\mu\kappa_i\kappa_j T}{N} \left(\frac{1-\omega_1}{1-\omega_2}\right)^T \int_{u_0^{ij}}^1 u^{-(1+T)} (1-u)^T [1 - (1-\omega_2)u]^{\tau-1} \left(1 - \frac{\omega_2 - \omega_1}{1-\omega_1} u\right)^{-1} du, \tag{39}$$

where u_0^{ij} is as in Eq. (14).

The integral in Eq. (39) diverges for $N \rightarrow \infty$, i.e., for $u_0^{ij} \rightarrow 0$. Therefore, we cannot consider its ‘‘large- N approximation’’ by setting $u_0^{ij} = 0$ as its lower limit. In particular, as shown for the case of $\omega_1 = \omega_2$, \bar{k}_{aggr} is sensitive to finite size effects, especially at larger network temperatures [4, 13], and to accurately compute it in general one needs to numerically evaluate the integrals

The above result holds true for any combination of $\omega_1, \omega_2 \in [0, 1)$. For $t \ll \tau$, $g_\tau(t) \approx 1$, and thus $r_{\text{ic}}(t)$, and consequently, the intercontact distribution $P_{\text{ic}}(t)$, decay according to the power law $1/t^{2-T}$. The scaling $P_{\text{ic}}(t) \propto 1/t^{2-T}$ is illustrated in Fig. 7. In the next section, we turn our attention to the expected time-aggregated degree.

VI. TIME-AGGREGATED DEGREE

To analyze the expected time-aggregated degree, we need to consider the probability that two nodes i and j with hidden degrees κ_i and κ_j and angular distance $\Delta\theta_{ij}$ do not connect during the observation period τ . This probability is given by

$$r_0(\kappa_i, \kappa_j, \Delta\theta_{ij}) = (1-p_{ij})[1 - (1-\omega_2)\tilde{p}_{ij}]^{\tau-1}, \tag{36}$$

where p_{ij} and \tilde{p}_{ij} are given by Eqs. (9) and (4).

The expected time-aggregated degree, denoted as \bar{k}_{aggr} , is given by

$$\bar{k}_{\text{aggr}} = (N-1)(1-r_0), \tag{37}$$

where r_0 is determined by removing the conditions on κ_i , κ_j , and $\Delta\theta_{ij}$ from Eq. (36),

$$r_0 = \int \int \int r_0(\kappa, \kappa', \Delta\theta) \rho(\kappa) \rho(\kappa') f(\Delta\theta) d\kappa d\kappa' d\Delta\theta. \tag{38}$$

Following the same procedure as before to remove the condition on $\Delta\theta_{ij}$, we can write

in Eqs. (39) and (38).

The above analysis is validated in Fig. 9. We see from the figure that \bar{k}_{aggr} decreases as the link persistence probability ω_1 increases, or as the network temperature T decreases. In particular, in sufficiently large networks, as ω_1 approaches 1 or T approaches 0, \bar{k}_{aggr} converges to the average snapshot degree \bar{k} . Further, we see that \bar{k}_{aggr} remains virtually unaffected by the non-link persis-

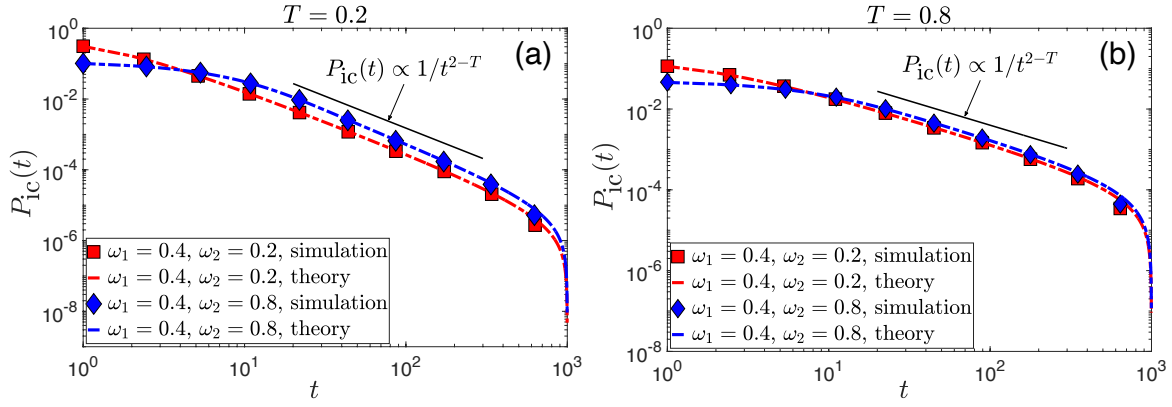


FIG. 7. Distribution of intercontact durations in simulated networks with the (ω_1, ω_2) -dynamic- S^1 model vs. theoretical predictions. The latter are given by $P_{ic}(t) = r_{ic}(t) / \sum_{j=1}^{\tau-2} r_{ic}(j)$, where $r_{ic}(t)$ is given by Eq. (34). Results are presented for two combinations of the persistence probabilities ω_1 and ω_2 . All other simulation parameters are the same as in Fig. 3.

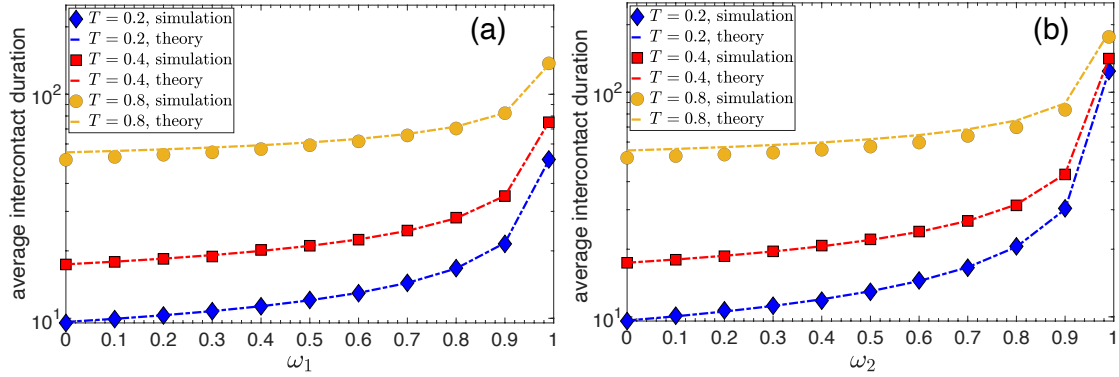


FIG. 8. Same as in Fig. 4, but for the average intercontact duration. The theoretical predictions (dashed lines) are given by $\bar{t}_{ic} = \sum_{t=1}^{\tau-2} t P_{ic}(t)$, where $P_{ic}(t)$ is computed as in Fig. 7.

	\bar{k}_{aggr}	\bar{t}_c	\bar{t}_{ic}
T	\nearrow^*	\searrow	\nearrow^*
ω_1	\searrow^*	\nearrow^*	\nearrow
ω_2	\searrow	\nearrow	\nearrow^*

TABLE I. Summary of dependencies of \bar{k}_{aggr} , \bar{t}_c , and \bar{t}_{ic} , on parameters T , ω_1 , and ω_2 . Arrows indicate an increase (\nearrow) or decrease (\searrow) of the corresponding average as T , ω_1 , or ω_2 increases. Stars indicate the averages that generally change more rapidly with a change in the corresponding parameter.

tence probability ω_2 . However, at the limit $\omega_2 \rightarrow 1$, \bar{k}_{aggr} tends again to \bar{k} . This explains why the performance of epidemic spreading processes may not be significantly affected by non-link persistence, unless it is extremely strong ($\omega_2 \rightarrow 1$).

Table I provides a summary of how \bar{k}_{aggr} , as well as the average contact and intercontact durations (\bar{t}_c and \bar{t}_{ic}) change with parameters T , ω_1 , and ω_2 .

VII. DISCUSSION AND CONCLUSION

We have generalized temporal random hyperbolic graphs by introducing distinct probabilities ω_1 and ω_2 for link and non-link persistence, and elucidated the non-trivial dependence of key temporal network properties on link and non-link persistence strength, and on the network temperature T . The generalized model can be used to study more diverse scenarios in the context of epidemic spreading and other dynamical processes running on temporal networks. This is because it allows more flexible tuning of the average contact and intercontact durations, and of the average time-aggregated degree. Specifically, these quantities are now controlled by three parameters (ω_1, ω_2, T) instead of two (ω, T) .

We have also proven that the tails of the contact and intercontact distributions decay as power laws with exponents $2 + T$ and $2 - T$, respectively, as in the case of $\omega_1 = \omega_2$ [13]. An outstanding question is whether there exists a simple model extension in which the tails of these distributions are not coupled by the common parameter T , but can be tuned more independently. An-

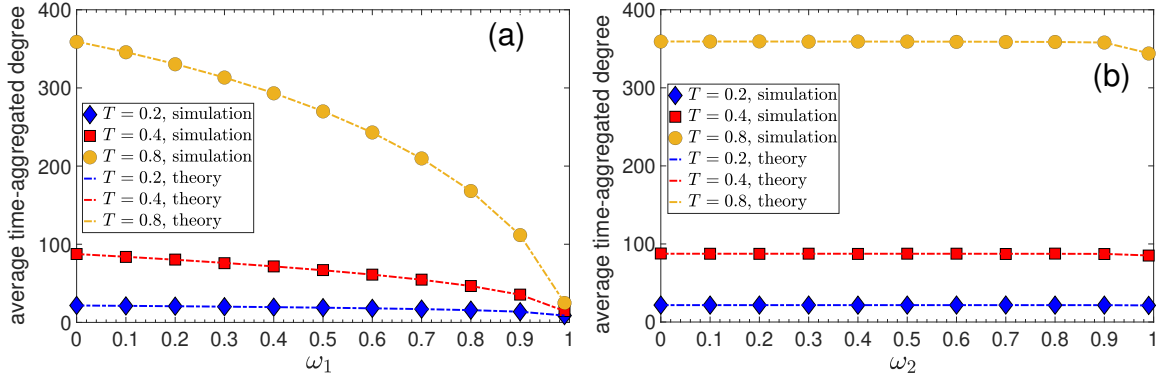


FIG. 9. Average time-aggregated degree vs. ω_1 , ω_2 , and T . Plot (a) shows the average time-aggregated degree as a function of the persistence probability of connections ω_1 . The persistence probability of disconnections, ω_2 , is set to zero. Results are shown for different values of the network temperature T . All other parameters are the same as in Fig. 3. The dashed lines depict theoretical predictions given by Eqs. (37)-(39). Plot (b) is similar to (a), except that ω_1 is set to zero, and we vary ω_2 .

other question is whether there exist model extensions in which the (inter)contact distributions deviate from pure power laws, as may be observed in real-world systems. Other interesting directions for future work include the derivation and analysis of models of temporal RHGs in higher dimensions [26], temporal RHG models where different pairs of nodes can have different link and non-link persistence probabilities [9], as well as temporal RHG models for bipartite networks [12, 27].

ACKNOWLEDGMENTS

The authors acknowledge support by the TV-HGGs project (OPPORTUNITY/0916/ERC-CoG/0003), co-funded by the European Regional Development Fund and the Republic of Cyprus through the Research and Innovation Foundation.

Appendix A: Appell F_1 series and Gauss hypergeometric function

In this section, we provide an overview of the Appell F_1 series and the Gauss hypergeometric function [14].

The Appell F_1 series is defined for $|x| < 1$ and $|y| < 1$ by

$$F_1(a, b_1, b_2, c; x, y) = \sum_{m=0}^{\infty} \sum_{n=0}^{\infty} \frac{(a)_{m+n} (b_1)_m (b_2)_n}{(c)_{m+n} m! n!} x^m y^n, \quad (\text{A1})$$

where $(q)_n$ is the Pochhammer symbol. For values of x and y outside the range $|x| < 1$ and $|y| < 1$, the function F_1 can be extended through analytic continuation [24]. Such continuations can be achieved by manipulating integral representations, similar to the one in Eq. (16), where changing the integration variable can allow the expression of the original F_1 series through another F_1 series,

e.g., see Eq. (17). Such transformations enable the definition of the F_1 series for a broader range of x and y .

The Gauss hypergeometric function is defined by the series

$${}_2F_1[a, b, c; z] = \sum_{n=0}^{\infty} \frac{(a)_n (b)_n}{(c)_n} \frac{z^n}{n!}, \quad (\text{A2})$$

for $|z| < 1$, and by analytic continuation elsewhere.

The Appell F_1 series $F_1(a, b_1, b_2, c; x, y)$ degenerates to the Gauss hypergeometric function when $x = y$,

$$F_1(a, b_1, b_2, c; x, x) = {}_2F_1[a, b_1 + b_2, c; x]. \quad (\text{A3})$$

Appendix B: Tail of the contact distribution for any $\omega_1, \omega_2 \in [0, 1)$

Here we establish that Eq. (28) in the main text holds true for any combination of $\omega_1, \omega_2 \in [0, 1)$. To this end, we utilize the transformation given by Eq. (1) in section 5.11 of Ref. [24], which states that

$$F_1[a, b, b', c; x, y] = (1-x)^{-b} (1-y)^{-b'} \times F_1[c-a, b, b', c; \frac{x}{x-1}, \frac{y}{y-1}]. \quad (\text{B1})$$

Applying this transformation to the F_1 function on the left-hand side of Eq. (25), allows us to rewrite h_1 as

$$h_1 = \omega_1^{t-1} \left(\frac{1-\omega_2}{1-\omega_1} \right) \times F_1[1-T, 1-t, 1, 3; 1 - \frac{1}{\omega_1}, \frac{\omega_2 - \omega_1}{1-\omega_1}]. \quad (\text{B2})$$

Now, using Eq. (23) with $a = 1 - T$, $b = 1$, $\lambda = -t$, $b' = 1$, $c = 3$, $x = 1 - \frac{1}{\omega_1}$, and $y = \frac{\omega_2 - \omega_1}{1 - \omega_1}$, we can write

$$\begin{aligned}
h_1 &= \omega_1^{t-1} \left(\frac{1-\omega_2}{1-\omega_1} \right) \sum_{n=0}^{m-1} \frac{(1-T)_n}{(3)_n} \left(\frac{\omega_2-\omega_1}{1-\omega_1} \right)^n {}_2F_1\left[1-t, 1-T+n, 3+n; 1-\frac{1}{\omega_1}\right] + O\left(\frac{1}{(-t)^{1-T+m}}\right) \\
&= \left(\frac{1-\omega_2}{1-\omega_1} \right) \sum_{n=0}^{m-1} \frac{(1-T)_n}{(3)_n} \left(\frac{\omega_2-\omega_1}{1-\omega_1} \right)^n {}_2F_1[2+T, 1-t, 3+n; 1-\omega_1] + O\left(\frac{1}{(-t)^{1-T+m}}\right). \tag{B3}
\end{aligned}$$

The last equality follows from Pfaff's transformation (Eq. (22) in section 2.1.4 of Ref. [24]), which states that

$${}_2F_1[a, b, c; z] = (1-z)^{-a} {}_2F_1\left[a, c-b, c; \frac{z}{z-1}\right]. \tag{B4}$$

We also utilized that ${}_2F_1[a, b, c; z] = {}_2F_1[b, a, c; z]$, which

follows from Eq. (A2).

Utilizing the asymptotic expansion for the hypergeometric function ${}_2F_1[a, b, c; z]$ for $|b| \rightarrow \infty$, given by Eq. (15) in section 2.3.2 of Ref. [24], we can express the ${}_2F_1$ function inside the sum in Eq. (B3), as

$$\begin{aligned}
{}_2F_1[2+T, 1-t, 3+n; 1-\omega_1] &= \left\{ \frac{\Gamma(3+n)}{\Gamma(1-T+n)} \frac{(1-\omega_1)^{-(2+T)}}{(t-1)^{2+T}} + \frac{\Gamma(3+n)}{\Gamma(2+T)} \frac{e^{-(1-\omega_1)(t-1)}}{[(1-\omega_1)(1-t)]^{1-T+n}} \right\} \\
&\quad \times \left[1 + O\left(\frac{1}{(1-\omega_1)(t-1)}\right) \right]. \tag{B5}
\end{aligned}$$

At large t the dominant term in Eq. (B5) is the first term

inside the brackets, and we can write

$${}_2F_1[2+T, 1-t, 3+n; 1-\omega_1] \approx \frac{\Gamma(3+n)}{\Gamma(1-T+n)} \frac{(1-\omega_1)^{-(2+T)}}{t^{2+T}}. \tag{B6}$$

Consequently, for large t we can approximate Eq. (B3) as

as

$$\begin{aligned}
h_1 &\approx \left(\frac{1-\omega_2}{1-\omega_1} \right) \frac{(1-\omega_1)^{-(2+T)}}{t^{2+T}} \sum_{n=0}^{\infty} \frac{(1-T)_n}{(3)_n} \left(\frac{\omega_2-\omega_1}{1-\omega_1} \right)^n \frac{\Gamma(3+n)}{\Gamma(1-T+n)} \\
&= \left(\frac{1-\omega_2}{1-\omega_1} \right) \frac{(1-\omega_1)^{-(2+T)}}{t^{2+T}} \frac{2}{\Gamma(1-T)} \sum_{n=0}^{\infty} \left(\frac{\omega_2-\omega_1}{1-\omega_1} \right)^n \\
&= \frac{2(1-\omega_1)^{-(2+T)}}{\Gamma(1-T)} \frac{1}{t^{2+T}}. \tag{B7}
\end{aligned}$$

We see that the above analysis also leads to Eq. (28). We validate the analysis in Fig. 10.

We note that in Eq. (B7), we let the summation run to infinity, since there is no single dominant term. The summation converges to $(1-\omega_1)/(1-\omega_2)$ when $|\frac{\omega_2-\omega_1}{1-\omega_1}| < 1$. This defines the region \mathcal{R}_2 of ω_1 and ω_2 , depicted in

Fig. 11, for which the above analysis holds. The union of \mathcal{R}_2 with \mathcal{R}_1 in Fig. 6 covers the full range of $\omega_1, \omega_2 \in [0, 1)$. Therefore, Eq. (28), and hence the scaling $P_c(t) \propto 1/t^{2+T}$, hold for any combination of ω_1 and ω_2 .

Proving Eq. (27). Equation (27) in the main text is obtained by using the same asymptotic expansion for

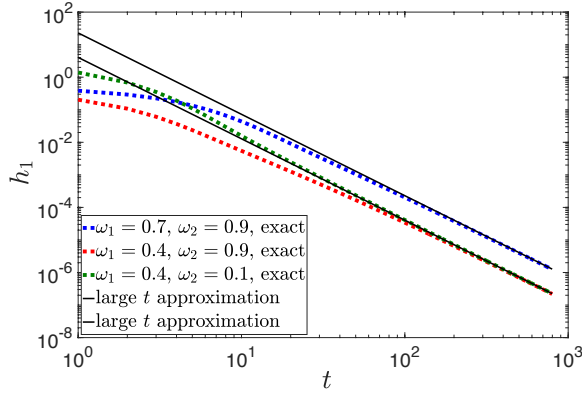


FIG. 10. Function h_1 in Eq. (B2) (dotted lines) vs. the approximation for large t in Eq. (B7) (solid lines). Results are shown for different values of ω_1 and ω_2 , while $T = 0.5$. All axes use a logarithmic scale.

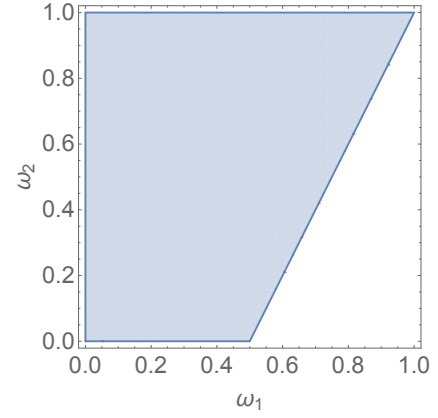


FIG. 11. Region $\mathcal{R}_2 := \{(\omega_1, \omega_2) \in \mathbb{R}^2 \mid |\frac{\omega_2 - \omega_1}{1 - \omega_1}| < 1\}$.

the hypergeometric function ${}_2F_1[a, b, c; z]$ for $|b| \rightarrow \infty$ as above (given by Eq. (15) in section 2.3.2 of Ref. [24]). Specifically, utilizing this expansion, we can write

$${}_2F_1\left[2 + T + n, 1 + t, 3 + n; 1 - \frac{1}{\omega_1}\right] = \left\{ \frac{\Gamma(3 + n)}{\Gamma(1 - T)} \frac{(1/\omega_1 - 1)^{-(2+T+n)}}{(t+1)^{2+T+n}} + \frac{\Gamma(3 + n)}{\Gamma(2 + T + n)} \frac{e^{-(1/\omega_1 - 1)(t+1)}}{[(1 - 1/\omega_1)(t+1)]^{1-T}} \right\} \times \left[1 + O\left(\frac{1}{(1/\omega_1 - 1)(t+1)}\right) \right]. \quad (\text{B8})$$

At large t , the dominant term in the above relation is

the first term inside the brackets. Utilizing also that ${}_2F_1[a, b, c; z] = {}_2F_1[b, a, c; z]$, we can write

$${}_2F_1\left[1 + t, 2 + T + n, 3 + n; 1 - \frac{1}{\omega_1}\right] \approx \frac{\Gamma(3 + n)(1/\omega_1 - 1)^{-(2+T+n)}}{\Gamma(1 - T)} \frac{1}{t^{2+T+n}}. \quad (\text{B9})$$

-
- [1] M. Starnini, A. Baronchelli, and R. Pastor-Satorras, Modeling human dynamics of face-to-face interaction networks, *Phys. Rev. Lett.* **110**, 168701 (2013).
 - [2] M. Starnini, B. Lepri, A. Baronchelli, A. Barrat, C. Cattuto, and R. Pastor-Satorras, Robust modeling of human contact networks across different scales and proximity-sensing techniques, in *Social Informatics* (Springer, Cham, 2017) pp. 536–551.
 - [3] M. A. Rodríguez-Flores and F. Papadopoulos, Similarity forces and recurrent components in human face-to-face interaction networks, *Phys. Rev. Lett.* **121**, 258301 (2018).
 - [4] F. Papadopoulos and M. A. Rodríguez-Flores, Latent geometry and dynamics of proximity networks, *Phys. Rev. E* **100**, 052313 (2019).
 - [5] D. Krioukov, F. Papadopoulos, M. Kitsak, A. Vahdat, and M. Boguñá, Hyperbolic geometry of complex networks, *Phys. Rev. E* **82**, 036106 (2010).
 - [6] F. Papadopoulos and S. Zambirinis, Dynamics of hot random hyperbolic graphs, *Physical Review E* **105**, 024302 (2022).
 - [7] X. D. Andrianou, C. Konstantinou, M. A. Rodríguez-Flores, F. Papadopoulos, and K. C. Makris, Population-wide measures due to the COVID-19 pandemic and exposure changes in the general population of Cyprus in March–May 2020, *BMC Public Health* **22**, 2279 (2022).
 - [8] M. A. Rodríguez-Flores and F. Papadopoulos, Hyperbolic mapping of human proximity networks, *Scientific Reports* **10**, 20244 (2020).
 - [9] P. Mazzarisi, P. Barucca, F. Lillo, and D. Tantari, A

- dynamic network model with persistent links and node-specific latent variables, with an application to the interbank market, *European Journal of Operational Research* **281**, 50 (2020).
- [10] F. Papadopoulos and K.-K. Kleineberg, Link persistence and conditional distances in multiplex networks, *Phys. Rev. E* **99**, 012322 (2019).
- [11] H. Hartle, F. Papadopoulos, and D. Krioukov, Dynamic hidden-variable network models, *Phys. Rev. E* **103**, 052307 (2021).
- [12] N. Friel, R. Rastelli, J. Wyse, and A. E. Raftery, Interlocking directorates in Irish companies using a latent space model for bipartite networks, *Proceedings of the National Academy of Science* **113**, 6629 (2016).
- [13] S. Zambirinis, H. Hartle, and F. Papadopoulos, Dynamics of cold random hyperbolic graphs with link persistence, *Phys. Rev. E* **106**, 064312 (2022).
- [14] F. W. Olver, D. W. Lozier, R. F. Boisvert, and C. W. Clark, *NIST Handbook of Mathematical Functions*, 1st ed. (Cambridge University Press, New York, USA, 2010).
- [15] M. J. Keeling and P. Rohani, *Modeling Infectious Diseases in Humans and Animals* (Princeton University Press, 2008).
- [16] M. Conti and S. Giordano, Mobile ad hoc networking: milestones, challenges, and new research directions, *IEEE Communications Magazine* **52**, 85 (2014).
- [17] A. Vazquez, B. Rácz, A. Lukács, and A.-L. Barabási, Impact of non-poissonian activity patterns on spreading processes, *Phys. Rev. Lett.* **98**, 158702 (2007).
- [18] T. Smieszek, A mechanistic model of infection: why duration and intensity of contacts should be included in models of disease spread, *Theoretical Biology and Medical Modelling* **6**, 25 (2009).
- [19] M. Karsai, M. Kivelä, R. K. Pan, K. Kaski, J. Kertész, A.-L. Barabási, and J. Saramäki, Small but slow world: How network topology and burstiness slow down spreading, *Phys. Rev. E* **83**, 025102 (2011).
- [20] A. Machens, F. Gesualdo, C. Rizzo, A. E. Tozzi, A. Barrat, and C. Cattuto, An infectious disease model on empirical networks of human contact: bridging the gap between dynamic network data and contact matrices, *BMC Infectious Diseases* **13**, 185 (2013).
- [21] L. Gauvin, A. Panisson, C. Cattuto, and A. Barrat, Activity clocks: spreading dynamics on temporal networks of human contact, *Sci. Rep.* **3**, 3099 EP (2013).
- [22] F. Papadopoulos, M. Kitsak, M. Á. Serrano, M. Boguñá, and D. Krioukov, Popularity versus similarity in growing networks, *Nature* **489**, 537 EP (2012).
- [23] M. Boguñá and R. Pastor-Satorras, Class of correlated random networks with hidden variables, *Phys Rev E* **68**, 036112 (2003).
- [24] H. Bateman, *Higher transcendental functions, [Volumes I-III]*, Vol. 1 (McGraw-Hill Book Company, 1953).
- [25] J. López, P. Pagola, and E. Pérez Sinusía, Asymptotics of the first Appell function F_1 with large parameters, *Integral Transforms and Special Functions* **24**, 715 (2013).
- [26] G. Budel, M. Kitsak, R. Aldecoa, K. Zuev, and D. Krioukov, Random hyperbolic graphs in $d + 1$ dimensions (2023), arXiv:2010.12303.
- [27] M. Kitsak, F. Papadopoulos, and D. Krioukov, Latent geometry of bipartite networks, *Phys. Rev. E* **95**, 032309 (2017).